The First Sino-US Joint Symposium on Multi-Scale
Analysis in Material Sciences and Engineering
Beijing, China, June 17-20, 2002

ADVANCES IN MICRO SCALE MODELING OF FAILURE MECHANISMS IN CERAMICS AND FIBER COMPOSITES

Horacio D. Espinosa and Sungsoo Lee

Department of Mechanical Engineering
Northwestern University, Evanston, IL 60208-3111, USA
E-mail: espinosa@northwestern.edu
http://www.mech.northwestern.edu/espinosa

Abstract. The present work is concerned with recent developments in computational modeling of advanced materials, such as ceramic materials and fiber reinforced composites. Numerical techniques of augmented finite element methods are provided for the analysis of dynamic behavior of materials subjected to wave propagation. Models that describe various mechanisms of dynamic failures at microscales are presented in some detail. Cohesive micro models for capturing dynamic fragmentation of ceramic microstructures and crack propagations in fiber composites materials are also presented. The cohesive laws are incorporated in interfaces and grain boundaries to capture crack nucleation, propagation, coalescence, interaction, and branching. Grain level micromechanical models are investigated while considering stochasticity of microstructures and sliding friction between bodies. Also discussed are numerical analyses utilizing the proposed models. Simulation results are contrasted with experimental observations.

Key words: Ceramic, Composite, Dynamic failure, Damage mechanics, Cohesive law

1 INTRODUCTION

Advanced materials, such as ceramics and fiber reinforced plastic (FRP) composites, are employed in various fields. Ceramic materials have many applications in civil and defense areas because of their low density, thermal properties and high compressive strength. For instance, ceramics are used in the machining of materials and in turbine engines; while in defense applications, ceramics are used in lightweight armor systems. Likewise, fiber reinforced plastic composites are also promising materials in applications of weight efficient aircrafts, submarine hubs, and armored vehicles.

In many applications, these advanced materials undergo dynamic loadings at high strain rates and, consequently, dynamic failure occurs in various forms, such as dynamic fracture, fragmentation, spallation, delamination, and ballistic penetration. Establishing structural integrity under dynamic conditions at high strain rates and post-failure behavior becomes a prerequisite for using advanced materials. However, many phenomena observed during deformation of the materials remain unanswered. The dynamic failure of advanced structural systems is very complex because of various mechanisms, such as large deformation, inelastic constitutive behavior, anisotropy, interfacial failure and subsequent contact/friction response. An insightful understanding of the interactions between these factors is important in estimating and improving the behavior of advanced materials for improved design of structural systems.

For the last decade, Espinosa and co-workers have extensively studied dynamic failure of advanced materials. A multiple-pane microcracking continuum damage model was developed based on homogenization of the cracked solid. The material response is captured by degrading its strength as microcracks growth on various orientations (Espinosa, 1995). This continuum model requires making assumptions on the initial size and distribution of microcracks and it cannot fully describe the growth of dominant cracks leading to macroscopic failure. To overcome these limitations, a discrete model that can reproduce nucleation, propagation and coalescence of cracks was developed (Espinosa et al., 1998a). This discrete model is based on a phenomenological framework in which the fracture characteristics of the material are embedded in a cohesive traction-displacement relation. Zavattieri and Espinosa (2001) have also performed grain level analysis applied to the modeling of microcracking of ceramics. Stochastic effects were included in these analyses and comparisons with experiments were carried out. Zavattieri and Espinosa (2002) have assessed the accuracy of the micromechanical models and its ability to reproduce experimental data. Likewise, the effect of the material microstructure on the material response was identified. A grain level micromechanical model was proposed to provide a tool toward understanding mechanisms that lead to macroscopic failure and to refine damage theories, which can be utilized in continuum models (Espinosa and Zavattieri, 2002a; 2002b).

Dynamic delamination in woven composites was also studied by Espinosa and co-workers with a 3D finite deformation anisotropic viscoplastic model in conjunction with contact/cohesive laws (Espinosa et al., 2000; Espinosa et al., 2001). These analyses showed that the model captures the constitutive response of woven GRP composites in confirmation with the experimental data. Dwivedi and Espinosa (2002) have later studied dynamic crack propagation in unidirectional Carbon/Epoxy composite through finite element analyses of asymmetric impact. Crack propagation is simulated by embedded interface elements along the possible crack path and contact/friction behind the crack tip is considered. Subsonic and intersonic crack propagation regimes were numerically predicted.

The present work reviews recent models and computational algorithms, which have been developed to analyze microcrack initiation and kinetics in ceramics, and delamination and crack propagation in composites materials. Numerical case studies are also presented to illustrate the applicability of the proposed models.

2 MODEL DESCRIPTION

This section presents finite element models developed to identify dynamic failure of ceramics and composites. A total Lagrangian finite element method is employed in the context of large deformation inelastic models.

2.1 Finite element computational model

A displacement based finite element formulation is obtained from the weak form at time t in Lagrangian coordinates as given by

$$\int_{B_0} \left[\nabla_{\mathbf{0}} \mathbf{T}^{\mathbf{0}} + \rho_0 (\mathbf{b_0} - \mathbf{a})\right] \cdot \eta dB_0 = 0 \tag{1}$$

$$\int_{B_0} \mathbf{T}^{\mathbf{0}} : \nabla_{\mathbf{0}} \eta dB_0 - \int_{B_0} \rho_0 (\mathbf{b_0} - \mathbf{a}) \cdot \eta dB_0 - \int_{S_{0\sigma}} \mathbf{t} \cdot \eta dS_0 = 0 \tag{2}$$

where $\mathbf{T^0}$ is the first Piola-Kirchhoff stress tensor, $\mathbf{b_0}$, $\mathbf{a}$, and $\mathbf{t}$ are the body force vector, acceleration vector, and boundary traction vector on volume B_0, and boundary $S_{0\sigma}$, respectively. Virtual displacement field η is assumed to be admissible, and ρ_0 is the material density per unit volume in the reference configuration. $\nabla_{\mathbf{0}}$ denotes the material gradient with respect to the reference configuration. The weak form of the momentum balance is given in terms of spatial quantities as

$$\int_{B_0} \boldsymbol{\tau} : \nabla^s \eta dB_0 - \int_{B_0} \rho_0 (\mathbf{b_0} - \mathbf{a}) \cdot \eta dB_0 - \int_{S_{0\sigma}} \mathbf{t} \cdot \eta dS_0 = 0 \tag{3}$$

where subscript s represents the symmetric part of the tensor, $\boldsymbol{\tau} = \mathbf{F}\mathbf{T^0}$ is the Kirchhoff stress, $\mathbf{F}$ is the deformation gradient and ∇^s stands for the spatial deformation tensor.

2.2 Finite deformation plasticity

The total deformation gradient $\mathbf{F}$ is decomposed into elastic and plastic parts as given by

$$\mathbf{F} = \mathbf{F^e}\,\mathbf{F^p} \tag{4}$$

Work conjugacy relations suggest plastic flow rules and elastic stress-strain relations,

$$\overline{\mathbf{L}}^p = \overline{\mathbf{L}}^p\left(\overline{\boldsymbol{\Sigma}}, \overline{\mathbf{Q}}\right), \quad \overline{\mathbf{T}}^0 = \overline{\mathbf{T}}^0\left(\overline{\mathbf{F}}^e\right) \tag{5}$$

where a tensor with a bar on its top denotes the tensor relative to the intermediate configuration $\overline{B}_t$ so that $\overline{\mathbf{L}}^p = \dot{\mathbf{F}}^p\left(\mathbf{F}^p\right)^{-1}$, $\overline{\boldsymbol{\Sigma}} = \left(\mathbf{F}^e\right)^T \mathbf{T}^0 \left(\mathbf{F}^p\right)^T$, $\overline{\mathbf{T}}^0 = \mathbf{T}^0\left(\mathbf{F}^p\right)^T$, and $\overline{\mathbf{Q}}$ represents a proper set of internal variables defined on the intermediate configuration $\overline{B}_t$. Here, $\overline{\boldsymbol{\Sigma}}$ is a stress measure conjugate to the plastic velocity gradient $\overline{\mathbf{L}}^p$ on $\overline{B}_t$.
The most general form consistent with the principle of material frame indifference is given by

$$\overline{\mathbf{T}}^0 = \mathbf{F}^e \overline{\mathbf{S}}\left(\overline{\mathbf{C}}^e\right) \tag{6}$$

and one constitutive law suitable for metals and polymers was proposed as,

$$\overline{\mathbf{S}} = \mathbf{L}\left(\frac{1}{2}\ln \overline{\mathbf{C}}^e\right) = \mathbf{L}\overline{\mathbf{H}}^e \tag{7}$$

in which $\mathbf{S}$ is the second Piola-Kirchhoff stress tensor, $\overline{\mathbf{C}}^e = \mathbf{F}^e\left(\mathbf{F}^e\right)^T$ is the elastic right Cauchy-Green deformation tensor in $\overline{B}_t$, $\overline{\mathbf{H}}^e$ is a logarithmic strain measure, and $\mathbf{L}$ is the material stiffness fourth order tensor. For an elastic isotropic solid, $\mathbf{L}$ is given by

$$\mathbf{L} = 2\mu\mathbf{I} + \left(k - \frac{2}{3}\mu\right)\mathbf{1} \otimes \mathbf{1} \tag{8}$$

such that μ, k, $\mathbf{I}$ and $\mathbf{1}$ are shear modulus, bulk modulus, identity fourth order tensor, and unity vector, respectively. It is required that the conjugate variables must be used in computation of constitutive laws.

The evolution of $\mathbf{F}^p$ follows the flow rule,

$$\dot{\mathbf{F}}^p = \overline{\mathbf{L}}^p \mathbf{F}^p, \; \overline{\mathbf{L}}^p = \mathbf{W}^p + \mathbf{D}^p \tag{9}$$

and assuming that $\mathbf{W}^p \equiv skew\overline{\mathbf{L}}^p = \mathbf{0}$ and $\mathbf{D}^p \equiv sym\overline{\mathbf{L}}^p = \dot{\boldsymbol{\varepsilon}}^p \overline{\mathbf{N}}$, the evolution equation is $\dot{\mathbf{F}}^p\left(\mathbf{F}^p\right)^{-1} = \dot{\boldsymbol{\varepsilon}}^p\overline{\mathbf{N}}$, where $\overline{\mathbf{N}}$ is the plastic flow direction and $\dot{\boldsymbol{\varepsilon}}^p$ is the effective plastic strain rate. In J2-flow theory, the direction of plastic flow is given by

$$\overline{\mathbf{N}} = \frac{3}{2}\frac{\overline{\mathbf{S}}_{dev}}{\overline{\sigma}} \tag{10}$$

and the effective stress is defined as a function of the deviatoric part of the second Piola-Kirchhoff stress tensor $\overline{\mathbf{S}}_{dev}$,

$$\overline{\sigma} = \sqrt{\frac{3}{2}\overline{\mathbf{S}}_{dev} : \overline{\mathbf{S}}_{dev}} \tag{11}$$

The effective plastic strain rate is a function of effective stress, temperature and internal variables, viz., $\dot{\boldsymbol{\varepsilon}}^p = f\left(\overline{\sigma}, T, \overline{\mathbf{Q}}\right)$ and, for instance, a commonly used formulation for a viscoplastic model is,

$$\dot{\boldsymbol{\varepsilon}}^p = \dot{\boldsymbol{\varepsilon}}_0^p\left[\left(\frac{\overline{\sigma}}{s(\boldsymbol{\varepsilon}^p, T)}\right)^{\alpha} - 1\right], \quad \overline{\sigma} > s, \qquad \dot{\boldsymbol{\varepsilon}}^p = 0, \quad \overline{\sigma} \le s \tag{12}$$

$$s(\overline{\boldsymbol{\varepsilon}}^p, T) = \sigma_0\left(1 + \frac{\overline{\boldsymbol{\varepsilon}}^p}{\overline{\boldsymbol{\varepsilon}}_0^p}\right)^{\frac{1}{\beta}}\left[1 - \left(\frac{T - T_0}{T_m - T_0}\right)^{\gamma}\right] \tag{13}$$

where s is material strength, σ_0 initial material strength, T_m melting temperature, T_0 reference temperature, α rate sensitivity, β hardening exponents and γ thermal softening exponents.

2.3 Anisotropic elastic model for ceramics

An elastic-anisotropic model is used to describe the grains single crystal behavior. The second Piola-Kirchhoff stress tensor, relative to the undeformed configuration, is described by

$$S_{ij} = C_{ijkl}H_{kl} \tag{14}$$

where $\mathbf{H} = (1/2)\ln\mathbf{C}$ is a logarithmic strain measure or Henky strain, $\mathbf{C} = \mathbf{F}\mathbf{F}^T$ is the elastic right Cauchy-Green deformation tensor, and C_{ijkl} is the elastic anisotropic material stiffness tensor in the global coordinates. In the case of anisotropic crystals, the elastic constitutive matrix $\hat{C}_{IJKL}$ is defined in the local coordinates of the grain by its principal material directions. For orthotropic materials, one of the principal material directions, which is selected randomly, must coincide with z-axis to keep the plane strain condition in x-y plane. The angle between the global axes x-y, and the two local axes for each grain lying in the plane x-y is generated randomly.

2.4 Anisotropic plasticity model for fiber composites

The constitutive relation of fiber reinforced composites is formulated in terms of the Green-Lagrange strain tensor $\mathbf{E}$ and the work conjugate, the second Piola-Kirchhoff stress tensor $\mathbf{S}$. A hyperelastic constitutive law yields,

$$\dot{S}_{ij} = C_{ijkl}\dot{E}_{kl}^e \tag{15}$$

such that $\dot{E}_{ij}^{e}$ is elastic component of Green-Lagrange strain rate tensor given by

$$\dot{E}_{ij}^{e} = \dot{E}_{ij} - \dot{E}_{ij}^{p} \tag{16}$$

And the plastic strain rate is obtained by the associate flow rule,

$$\dot{E}_{ij}^{p} = \dot{\lambda}\frac{\partial f}{\partial S_{ij}} \tag{17}$$

in which f is flow potential and $\dot{\lambda}$ plastic rate proportionality factor. The inelastic behavior of the composite is modeled based on flow potential quadratic in the second Piola-Kirchhoff stress tensor,

$$\begin{aligned}2f\left(S_{ij}\right) = {} & a_{11}S_{11}^{2} + a_{22}S_{22}^{2} + a_{33}S_{33}^{2} + 2a_{12}S_{11}S_{12} + 2a_{13}S_{11}S_{33} + 2a_{23}S_{33}S_{22} \\ & + 2a_{44}S_{23}^{2} + 2a_{55}S_{13}^{2} + 2a_{66}S_{12}^{2}\end{aligned} \tag{18}$$

When the load is applied in the fiber directions, it is observed that woven fiber composites behave linearly up to failure so that $E_{11}^{p} = E_{22}^{p} = 0$ and the yield function is given by

$$f\left(S_{ij}\right) = \frac{1}{2}S_{33}^{2} + a_{44}S_{23}^{2} + a_{55}S_{13}^{2} + a_{66}S_{12}^{2} \tag{19}$$

In the case of equal fiber volume fractions in the principal directions 1 and 2, $a_{44} = a_{55}$ can be used to simplify the flow potential as,

$$f\left(S_{ij}\right) = \frac{1}{2}S_{33}^{2} + a_{44}\left(S_{23}^{2} + S_{13}^{2}\right) + a_{66}S_{12}^{2} \tag{20}$$

If loading is in the transverse direction, it is shown that the behavior of woven fiber composites is almost linear, i.e., $E_{33}^{p} = 0$. Hence, the flow potential is reduced to,

$$f\left(S_{ij}\right) = a_{44}\left(S_{23}^{2} + S_{13}^{2}\right) + a_{66}S_{12}^{2} \tag{21}$$

For unidirectional fiber reinforced carbon/epoxy composite with 2-3 isotropy, 1 being the fiber direction and 2 normal to it in the lamina plane, Equation (18) reduces to,

$$f\left(S_{ij}\right) = \frac{1}{2}S_{22}^{2} + a_{66}S_{12}^{2} \tag{22}$$

The rate of plastic work is given by

$$\dot{W}^{p} = S_{ij}\dot{E}_{ij}^{p} = \bar{S}\dot{\bar{E}}^{p}, \quad \bar{S} = \sqrt{3f} \tag{23}$$

where the bar denotes the effective value. The proportionality factor is obtained by

$$\dot{\lambda} = \frac{3\dot{\bar{E}}^{p}}{2\bar{S}} \tag{24}$$

The effect of strain rate and temperature is modeled by

$$\dot{\bar{E}}^{p} = \dot{\bar{E}}_{0}^{p}\left[\frac{\bar{S}}{g\left(\bar{E}^{p},T\right)}\right]^{m} \text{ if } \bar{S} > g\left(\bar{E}^{p},T\right), \quad g\left(\bar{E}^{p},T\right) = \bar{S}_{y}\left[1 - \left(\frac{T - T_{0}}{T_{m} - T_{0}}\right)^{\alpha}\right] \tag{25}$$

where $\overline{S}_y$ is flow stress at reference plastic strain rate $\dot{\overline{E}}_0^p$ and temperature T_0, and $\overline{S}$ is flow stress at current plastic strain rate $\dot{\overline{E}}^p$ and temperature T. T_m is the matrix transition temperature, m is the rate sensitivity exponent, and α is the temperature sensitivity exponent. Experiments suggest that the referenced flow stress can be defined by $\overline{S}_y = \left(\overline{E}^p / A\right)^{1/n}$ in which n is the strain hardening exponent.

2.5 Mesh adaptivity

Element distortion in Lagrangian dynamic finite element simulations results in a dramatic increase of calculation time and failure to capture large inelastic deformation behavior. For the case of excessive distortion of element, field variables may not be interpolated accurately, and therefore numerical errors may accumulate drastically. A solution for overcoming this drawback is to re-discretize the domain with an undistorted mesh and to continue the calculation. Adaptive mesh optimization is used with a mesh transfer operator that depends on the material constitutive behavior (Espinosa et al., 1998b; 2001). The objective function is the quality of element, Q_k, which evaluates the element shape and size, given by

$$Q_k = \alpha \frac{V_k}{P_k} \exp\left[-\beta^2 \ln^2\left(\frac{h_k}{h^*} \right) \right] \tag{26}$$

where V_k is the area, P_k is the perimeter, h_k is $P_k/3$ in this case, and h^* is the desired size of element k. In the region where deformation occurs rapidly, more elements are employed based on the rate of plastic work, $\dot{W}^p = \sigma \dot{\varepsilon}^p$. The quality of mesh is defined by the quality of its worst element as $Q_{global} = \min_k Q_k$. To provide better quality, the submesh formed by the worst element and its neighbors can be remeshed.

Another method for improving the quality of mesh is *topological* mesh optimization, which is based on several operations of trial-and-error until a higher quality mesh is formed. The operations consist of defining a cluster, removing its interior node, connecting all the edges in the cluster boundary to one of the boundary nodes, or connecting them to a node at its center. However, this method does not allow the nodes to move and it is likely there will be some elements deformed after remeshing. *Geometrical* mesh optimization that allows the movement of nodes has been performed (Espinosa et al., 1998b). Only the position of the nodes which belong to the worst element and their neighbor nodes are modified to maximize the objective function Q_{global}.

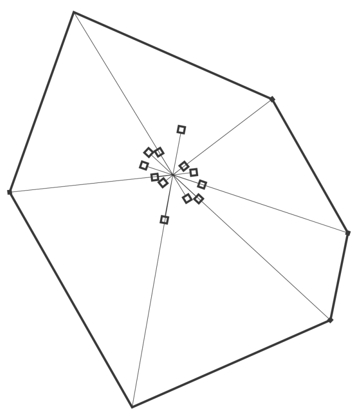

Figure 1: Sampling positions for local geometrical optimization in 2-D.

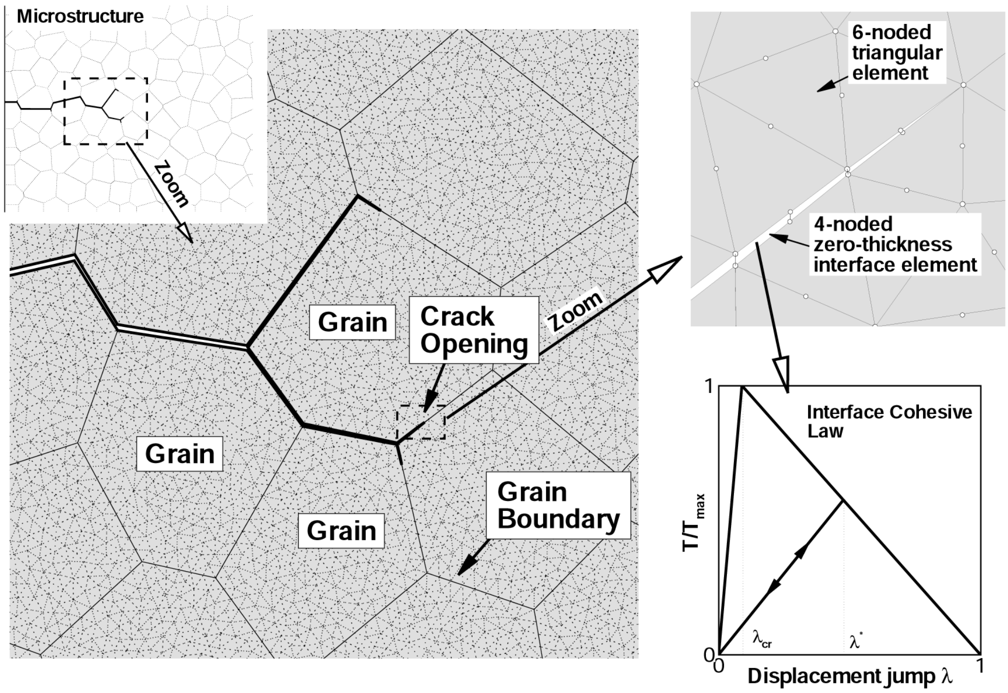

Figure 2: Schematics of cracking in interface elements using an irreversible interface cohesive law.

Since the min type function is not differentiable, a simple node-by-node algorithm is used. After the selecting quality is evaluated, an updated position is chosen which maximizes the quality. Figure 1 shows relocating a node to a set of sampling positions in 2-D local geometrical optimization.

2.6 Cohesive laws

A contact/interface algorithm implementing interface cohesive laws is used to describe the kinematics, contact, friction, crack initiation, and crack propagation at interfaces. As shown in Figure 2, interface elements, whose behavior is governed by cohesive laws, are embedded along the possible crack path, grain boundaries, or interfaces between two different materials to analyze the cohesive interaction and failure. A contact model (Espinosa et al., 1998b) is integrated with interface elements to simulate crack initiation, subsequent large sliding, and opening and closing of the interface. The interface cohesive law describes the evolution of the tensile and shear tractions in zero thickness interface elements as a function of relative normal and tangential displacement jumps. Compressive tractions are calculated with the impenetrability condition employed in the contact module.

The model assumes that the interface carries forces that oppose separation and shear between the surfaces until debonding. The magnitude of these forces is a function of the relative separation and shear displacements between the two surfaces. In formulating the cohesive law, a non-dimensional effective displacement jump is defined by

$$\lambda = \sqrt{\left(\frac{u_n}{\delta_n}\right)^2 + \xi^2\left(\frac{u_t}{\delta_t}\right)^2} \tag{27}$$

where u_n and u_t are actual normal and tangential displacement jumps at the interface estimated by the finite element analysis, and δ_n and δ_t are critical values at which interface failure takes place. For a triangular $T-\lambda$ law (see Figure 2), the normal and tangential components of the traction vector are given by

$$T_n = \frac{u_n}{\delta_n}\frac{T_{\max}}{\lambda_{cr}}, \quad T_t = \alpha \frac{u_t}{\delta_t}\frac{T_{\max}}{\lambda_{cr}} \quad (0 \le \lambda \le \lambda_{cr}) \tag{28}$$

$$T_n = T_{\max}\frac{u_n}{\delta_n}\frac{1-\lambda}{\lambda(1-\lambda_{cr})}, \quad T_t = \alpha T_{\max}\frac{u_t}{\delta_t}\frac{1-\lambda}{\lambda(1-\lambda_{cr})} \quad (\lambda_{cr} < \lambda \le 1, \text{ loading}) \tag{29}$$

$T_{\max}$ is the maximum normal traction that the interface can develop before failure and $\alpha = \xi^2(\delta_n/\delta_t)$ is the parameter coupling the normal and shear tractions, such that $\xi^2 = G_{\mathrm{IIc}}/G_{\mathrm{Ic}}$. It is assumed that the traction increases linearly to its maximum value $T = T_{\max}$ when $\lambda = \lambda_{cr}$. Beyond λ_{cr}, the traction reduces to zero linearly until the maximum displacement jump, when $\lambda = 1.0$, and any unloading takes place irreversibly. Hence, the interface between bodies is intact until the interface traction reaches the maximum value. Once the maximum traction is reached at a specified critical effective displacement jump, the interface starts deteriorating. The value of λ_{cr} is selected such that the wave speeds in the material with interfaces are the same as the ones without interfaces during reversible loading. The initial slope $T_{\max}/(\lambda_{cr}\delta)$ in the $T-\delta$ diagram has to be large enough to obtain proper wave speeds of the material but not so large as to provoke numerical instabilities (Espinosa and Zavattieri, 2002a; 2002b). From the values of fracture toughness K_{Ic}, or equivalently G_{Ic}, assuming plane strain, and the maximum interface stress, the critical interface displacement jump is computed by equating the area under the $T-\delta$ diagram to G_{Ic}. As soon as the effective displacement jump reaches 1.0, the interface element is assumed to have failed totally and the two surfaces sharing the interface element separate, i.e., a debonding occurs and a crack initiates. Consecutive failure of the neighboring interface elements simulates crack propagation and coalescence. Thereafter, the interaction between the surfaces is described only by the contact algorithm, including frictional effects. The compressive tractions at the interfaces are calculated either with the compressive part of the $T-\delta$ relationship or through the impenetrability condition employed in the contact model, depending on whether there are large displacements.

2.7 Generation of polycrystalline microstructures

A grain level micromechanical model is used to analyze polycrystalline brittle materials. As shown in Figure 3(a), a real ceramic microstructure is obtained from digitization of an SEM micrograph. After digitization, grains are represented by individual polygons and a mesh is generated inside each polygon with triangular elements generated by Delaunay triangulation. Grain boundaries are set by interface elements along the polygon edges such that the nodes belonging to the interface elements are the nodes of the adjacent triangular elements on the polygon boundaries.

To study the effect of grain morphology, different microstructures are reproduced by Voronoi tessellation, which is widely used in simulating grain structures in polycrystalline materials. For two-dimensional cases, Voronoi tessellation divides a plane into grain-like polygons corresponding to nuclei that may be thought as nuclei of grains. A cloud of nuclei are generated and distributed randomly in a specified area. Since the number and distance between nuclei determine grain sizes and shapes, distribution of nuclei must be monitored to control the grain sizes. Note that the nuclei closer to the borders of the area may not have sufficient numbers of neighboring nuclei to form a complete polygon. Such incomplete polygons and the Voronoi diagram define the open Voronoi tessellation. A special treatment on the microstructure boundary has

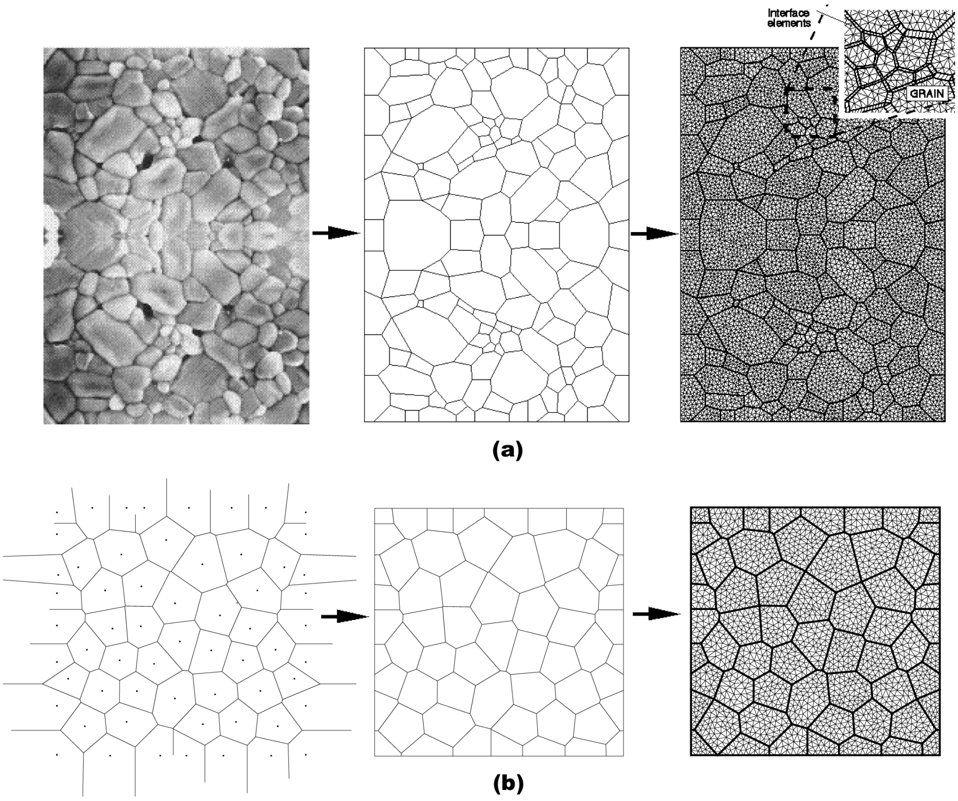

Figure 3: (a) Mesh generations from digitization of an actual microstructure, (b) mesh generation from Voronoi tessellation.

to be made to obtain the closed Voronoi tessellation. Each polygon is named a Voronoi cell and represents an individual grain that is meshed using Delaunay triangulation. Also, interface elements are inserted along the grain boundaries. Figure 3(b) shows Voronoi tessellation and a finite element mesh for the grain model (Espinosa and Zavattieri, 2002a; 2002b).

3 CASE STUDIES

3.1 Grain level modeling of fragmentation in ceramics

To examine the effect of ceramic microstructure on macroscopic failure signatures here we introduce a plate impact configuration we have used in the simulations. The configuration of a soft-recovery normal impact experiment is shown in Figure 4(a). Microcracking is induced by a tensile pulse originating from an intentional gap manufactured between the specimen and the momentum trap upon reflection of the compressive pulse. The velocity-time profiles recorded at the rear surface of the momentum trap provide information on microcrack initiation and evolution. The Lagrangian *t-X* diagram is shown in Figure 4(b) to visualize the conditions induced in the plates following impact. In the case of brittle materials, the tensile region 4 in Figure 4(b) is the site where microcracking occurs. When spallation initiates, the release waves emitted from the newly formed free surfaces significantly change the pattern of waves inside of the specimen. The pull-back signal is measured right after the first compressive pulse as an indicator of damage kinetics. The shape of the pull-back signal and second compressive pulse reflects both microcracking within the specimen and attenuation of the longitudinal wave while traveling through the already damaged material. Specimen recovery is achieved, which is key to physically identifying a unique solution to this highly nonlinear problem.

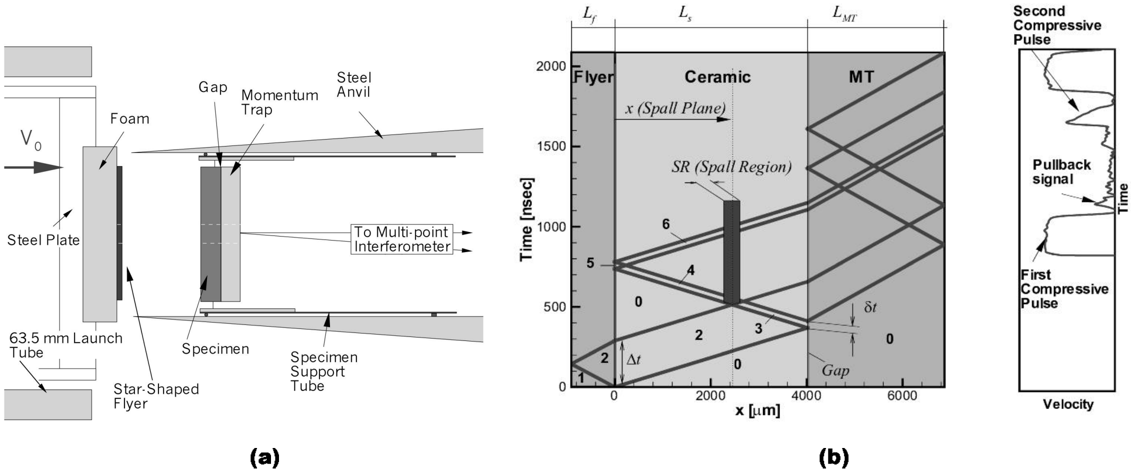

Figure 4: (a) Configuration of soft-recovery impact, (b) Lagrangian t-X diagram.

Because the primary damage mode in this experiment is spallation due to the low impact velocities, a representative volume element (RVE) at the spall region is considered for the analysis; see Figure 5. The top and bottom boundaries are modeled through viscous boundary conditions, which represent the exact elastic solution, while the side boundaries are periodic. To reproduce the particle velocity observed in the experiment reported in Figure 6, Shot 88-04, the effects of the following features were investigated: (1) a Weibull distribution of the interfacial strength $T_{\max}$ and fracture toughness K_{Ic} along the grain boundaries, (2) realistic microstructures considering grain morphology and size distributions, (3) size of RVE, and (4) rate of failure in the grain boundaries. In the reported experiment, the impact velocity is $V_0 = 48.4\,\mathrm{m/s}$ and the pulse duration is 70 ns. The maximum compressive axial stress is 614 MPa. Figure 6 shows an experimental result of particle velocity recorded at the rear surface of momentum trap and the comparison with a numerical result. In the numerical simulation, an RVE of 300 μm was considered and a mesh having a non-uniform distribution of grain sizes and shapes was used as shown in Figure 7. Interfacial strength and fracture toughness of the grain boundaries were given by a Weibull distribution with $T^0_{\max} = 5\mathrm{GPa}$, $K^0_{\mathrm{Ic}} = 2\mathrm{MPa}\cdot\mathrm{m}^{1/2}$ and $m = 3$. The evolution of the microcracks is shown in Figure 7. The numerical results are in excellent agreement with the most significant feature of the experiment, which are the pull-back signal amplitude and shape. Also, the simulation reproduces the attenuation of the second compressive pulse as

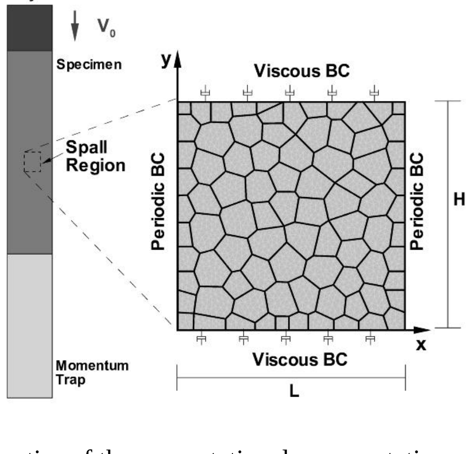

Figure 5: Schematics of the computational representative volume element.

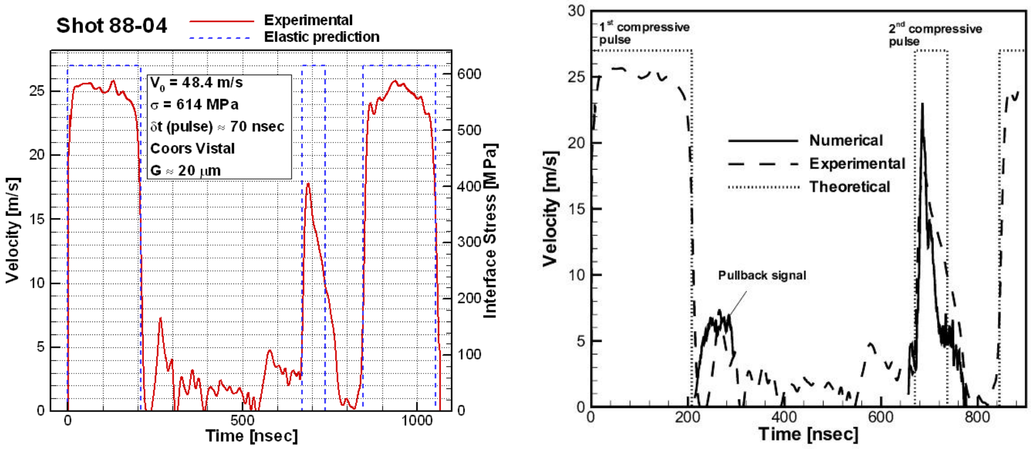

Figure 6: Experimental particle velocity and comparison between numerical simulation

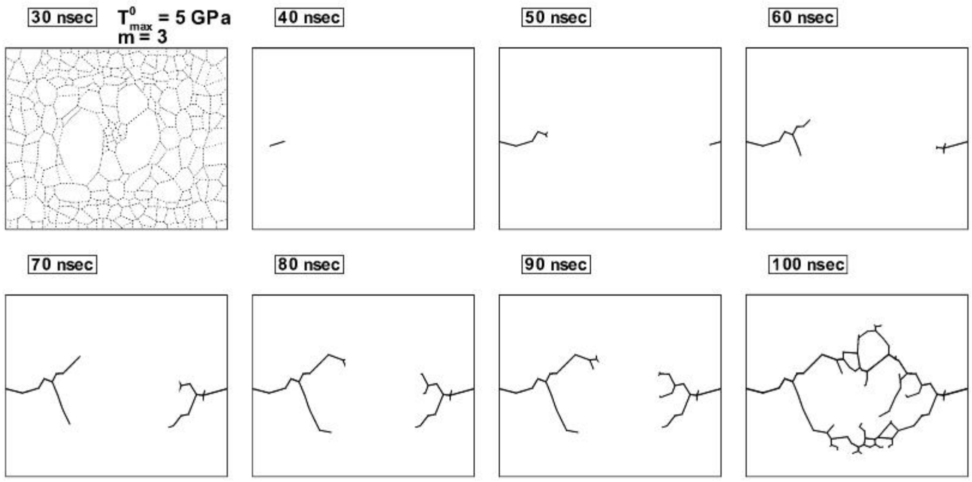

Figure 7: Evolution of crack pattern

observed in the experimental results. It is noticeable that grain morphology and strength distribution play key roles in capturing the proper microcrack initiation and fragmentation kinetics, i.e., crack speed and path in real microstructures. On the other hand, Zavattieri and Espinosa (2001) showed that rate effects in grain boundary failure can reproduce the velocity histories but it is inconsistent with observed damage patterns in recovered samples. They also showed that if grain morphology is not accounted for, the failure kinetics is not properly modeled.

3.2 Dynamic friction at high sliding velocities in ceramics

The normal impact soft recovery experiments have been extended to pressure-shear impact soft recovery experiments to study the dynamic shearing resistance of materials and dynamic friction. This experimental technique provides unique capabilities in characterizing damage and inelasticity of advanced materials under dynamic loading conditions. The configuration of the pressure shear experiment is shown in Figure 8 and experimental results are shown in Figure 9. Numerical simulations are required for interpreting failure mechanisms and kinetics due to the impossibility of recovering intact ceramic specimen after applying stresses high enough to initiate damage. It is also difficult to obtain a full understanding of the failure mechanisms of ceramics by observing only the velocity histories.

Simulations accounting for the contact and frictional sliding between flyer, target and

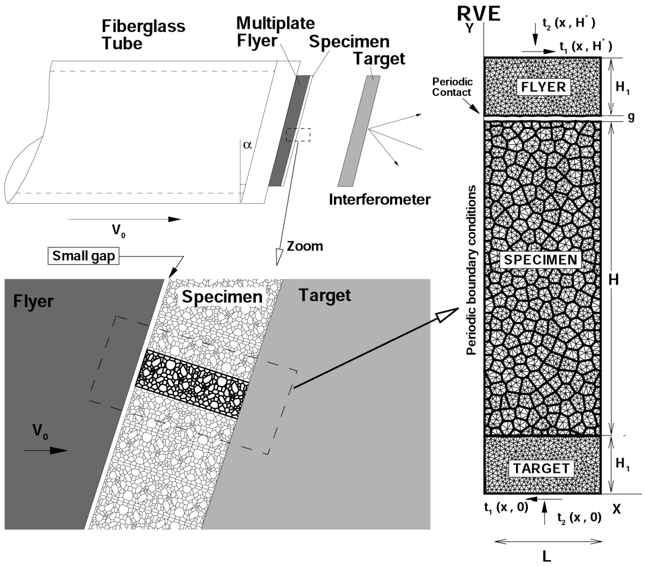

Figure 8: Schematics of experimental configuration and representative volume element for calculation

specimen plates including surface roughness were performed with a multi-body contact algorithm (Zavattieri and Espinosa, 2002). The calculation involved the modeling of flyer and target plates, including roughness of the surfaces in contact and various material inelasticity mechanisms. Interface elements and cohesive laws accounting for intergranular microcracking were used to model the ceramics. The parameters for interfacial strength were selected statistically by means of Weibull distributions. To account for the heat generated by plastic work in the target plate, a temperature-dependent visco-plasticity model and heat conduction were included in the modeling of the steel plates. Adaptive refinement/coarsening remeshing was used to accommodate the large deformations in the steel plates.

Numerical studies were performed to simulate the experiment 7-1025 with initial flyer velocity $V_0 = 148\,\text{m/s}$ and inclination angle $\alpha = 18°$. The study showed that plastic deformation of metal asperities, due to the frictional sliding near the surfaces, is the dominant deformation mechanism. Figure 9 shows the transverse velocity obtained from the experimental data, the simulation neglecting friction sliding, and the simulation considering surface roughness, contact and friction. The latter captures a peak transverse velocity of about 20 m/s while the former, omitting friction effects, shows a velocity of about 45 m/s strongly overpredicting the transferred shear wave. In

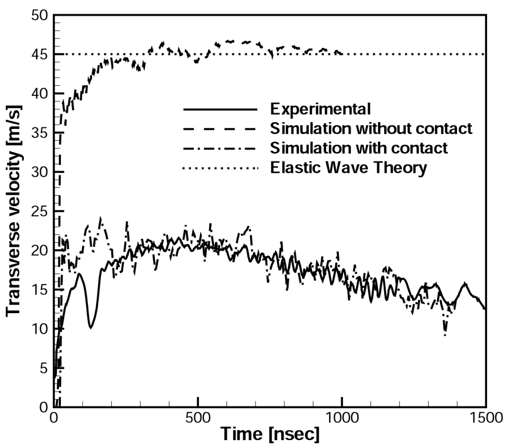

Figure 9: Transverse velocity obtained by experiments, simulation without considering contact between ceramic and target, and simulation including surface roughness and contact

addition, the gradual reduction of the velocity after 500 ns can be observed in the simulation accounting for frictional sliding, which is consistent with the experimental results. Prior to full scale simulations, parametric studies were performed to understand the effects of (1) various surface roughness profiles in ceramic and target plates, (2) material properties of the target plate, and (3) grain boundaries strength in the ceramic. It was found that plasticity, rate dependence, and thermal softening in steel plates are all mechanisms contributing to the observed transverse velocity histories. Full scale simulations that consider all the key factors examined in the parametric studies were conducted. Figure 10(a) shows the RVE finite element model with surface roughness and a gap between the flyer and the specimen plates. As shown in the evolution of crack pattern, see Figure 10(b), most of the microcracks initiate at the ceramic surface and propagate towards the inside of the specimen. The normal and transverse velocity histories are compared with the experimental data as shown in Figure 11. It is observed that both velocity histories obtained by numerical simulations are in good agreement with the experimental results. This work provides tools and means to understand the macroscopic bulk and surface responses of brittle materials when subjected to dynamic multi-axial loading at the micrometer scale. The computational method is very useful in identifying dominant failure modes and, particularly, in the study of dynamic friction of brittle and ductile materials.

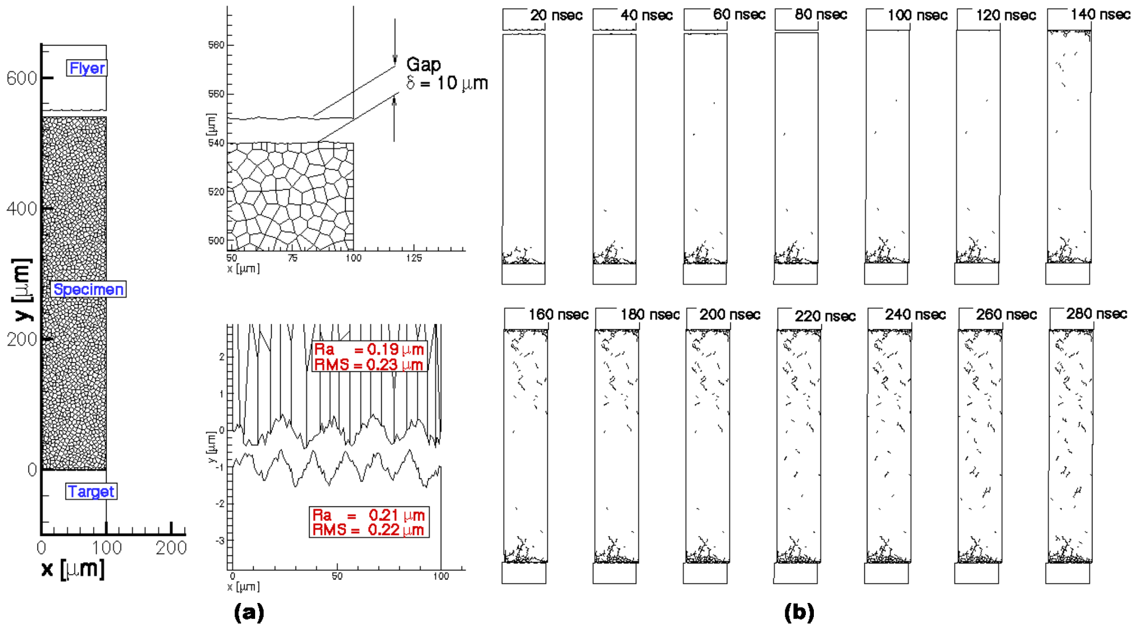

Figure 10: (a) Mesh with average grain size of 2μm and surface roughness for full scale pressure-shear simulation (b) microcrack pattern in the ceramic specimen

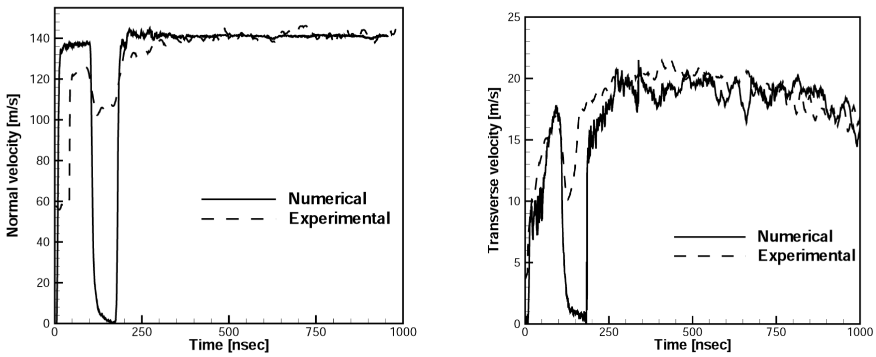

Figure 11: Comparison of velocity histories obtained from full scale simulation and experiment

3.3 Damage evolution in GRP composites subjected to impact loading

The finite deformation anisotropic visco-plasticity model discussed in Section 2.4 is utilized to study the constitutive relation of a woven fiber reinforced plastic composite material and its behavior under impact loading. The model parameters are determined by off-axis tension tests, compression tests, and out-of-plane shear experiments (Espinosa et al., 2001). Numerical analyses of off-axis tension tests and compression tests under plane stress were performed to validate the presented anisotropic visco-plastic model. Figure 12 shows the finite element mesh used in the off-axis tension simulation and the results obtained by experiments and numerical simulations in five different fiber directions. Figure 13 shows the finite element mesh used in the simulation of compression test and the comparison of experimental results with numerical predictions. The computational analyses are in good agreement with the experimental results.

To simulate ballistic penetration experiments, the computation model is enhanced with mesh adaptivity and contact/interface elements using cohesive laws. The anisotropic visco-plasticitiy model is used to model inelasticity within each lamina, while accounting for fiber directions, rate effects, and large deformation effects, which includes large displacements and rotations of laminae. Interaction between laminae before and after delamination and interply inelasticity are simulated by interface cohesive

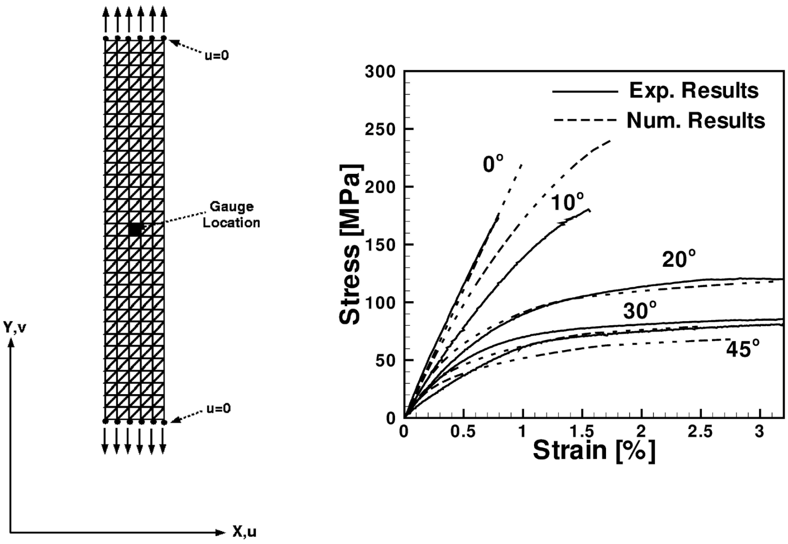

Figure 12: Finite element mesh and off-axis test results obtained by simulations and experiments.

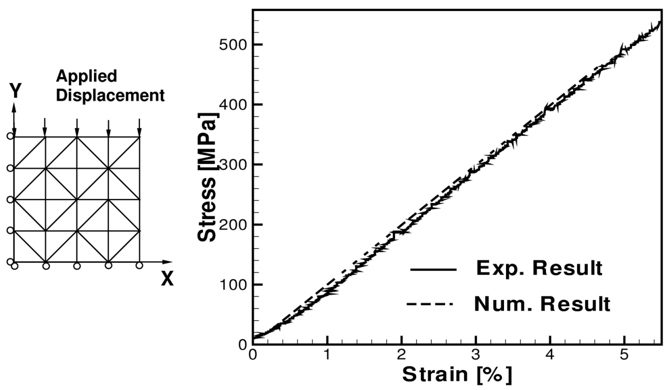

Figure 13: Finite element mesh and compression test results obtained by simulations and experiments.

elements embedded between laminae. Mesh adaptivity is implemented to overcome the problems resulted from excessive mesh distortion at regions where large deformation occurs. A consistent mesh transfer operator was derived for this purpose (Espinosa et al., 2001).

The anisotropic visco-plastic model is used assuming the plate consists of 1, 10, 20 and 40 laminae to analyze the role of delamination in energy absorption mechanisms, as shown in Figure 14. An anisotropic elastic model is used with a 40 laminae plate to discern the effect of pure delamination. To understand the energy absorption phenomenon, modes of energy dissipation are analyzed. Figure 15 shows the history of total internal energy and kinetic energy in the GRP target. The internal energy stored in the target is maximum in the calculation of one lamina without interface elements. There is no noticeable difference in the kinetic energies for the 10, 20, 40 laminae cases. Figure 16(a) suggests that significant amount of internal energy is dissipated in the inelastic deformation of the GRP laminae. As expected, the delamination energy increases as the number of laminae increases, as shown in Figure 16(b). It is expected that the proposed model would provide a valuable computational tool for the analyses of inelasticity and delamination in fiber composites.

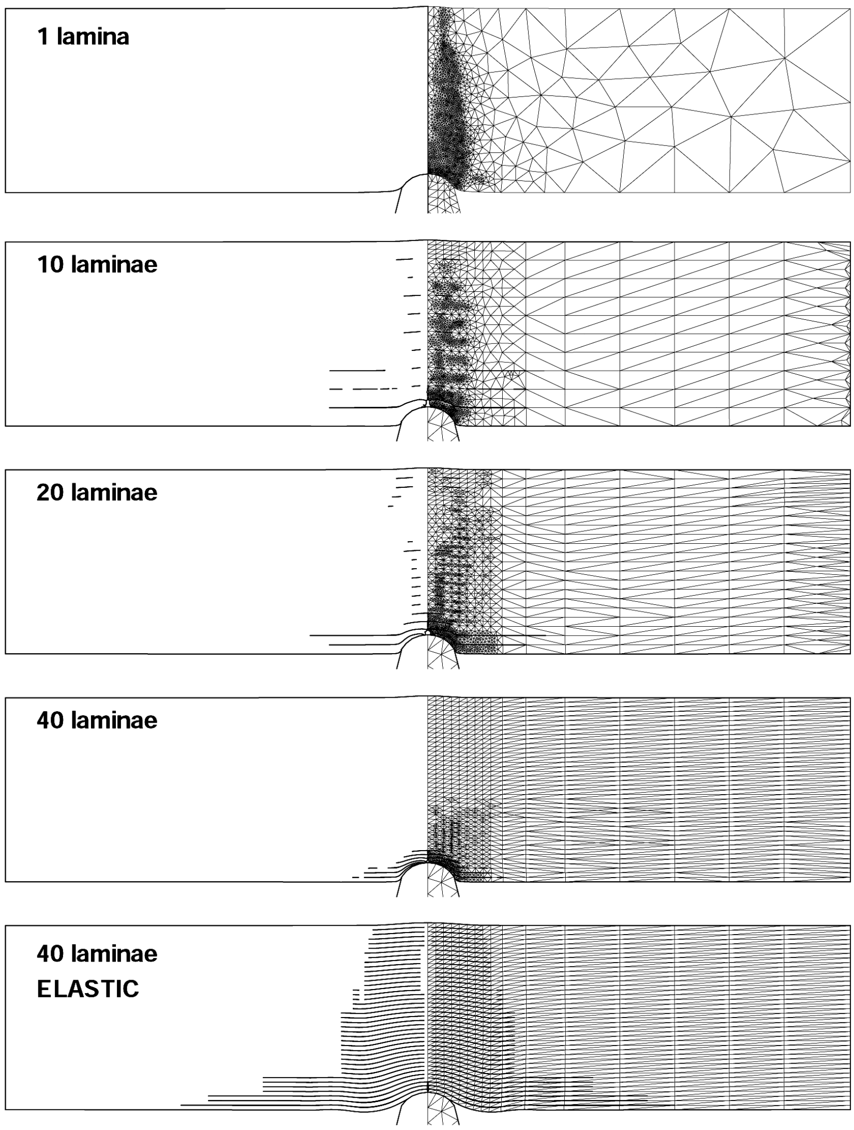

Figure 14: Plane strain FEM simulation of ballistic penetration in GRP plates with 1, 10, 20, and 40 laminae. The thick lines in the left half depict delamination between laminae.

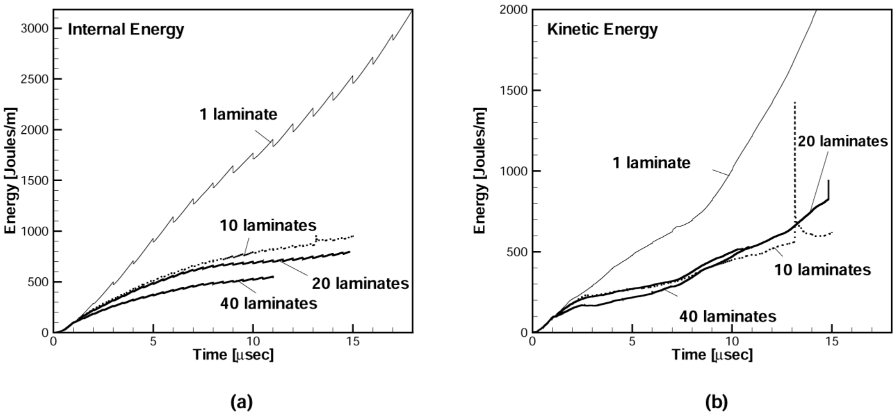

Figure 15: (a) Internal energy history of GRP plate (b) kinetic energy history of GRP plate.

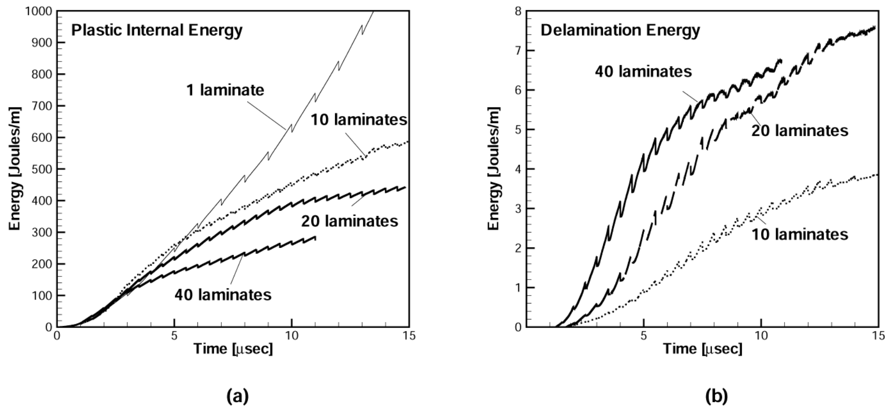

Figure 16: (a) Plastic energy history of GRP plate (b) delamination energy history of GRP plate.

3.4 Dynamic crack propagation in unidirectional composite materials

In recent years, the significance of studying dynamic crack propagation has increased because (1) increasing interests on multi-layered materials in civilian and defense applications, (2) endeavors to determine overall behavior and damage mode of advanced materials resulting from dynamic crack propagation, and (3) experimental observations showing that the velocity of a dynamic crack along a bimaterial interface can be intersonic. The importance to develop tools for finite element analyses of dynamic crack propagation in fiber composite materials subjected to impact loading is here discussed and illustrated. In particular, intersonic crack propagation is investigated with the following aspects in mind: (1) threshold impact energy beyond which intersonic crack propagation can be achieved, (2) effects of plastic zone around the crack tip, (3) formation of shock waves, (4) characteristics of contact zone behind the crack tip, (5) frictional effects in the contact zone, and (6) characterization of intersonic crack propagation in terms of the dynamic J' integral to study the associated energy flux.

Finite element analyses were conducted to study dynamic crack propagation in unidirectional graphite/epoxy composites using a cohesive interface formulation and a contact/friction algorithm (Dwivedi and Espinosa, 2001; 2002). A total Lagrangian code was used with a finite deformation anisotropic visco-plastic model discussed in Section 2.4. It was shown that a model combining a homogenized constitutive relation for anisotropic fiber composite materials and a cohesive interface law between laminae can be employed to analyze dynamic delamination. Simulations were performed at various impact velocities and surface friction characteristics. The dynamic J' integral was evaluated in each case to characterize the dynamic stress field and energy associated with the propagating crack tip. Using the weight function q, the dynamic J' integral is given by

$$J' = \int_{A_0}\left[P_{ji}\frac{\partial U_i}{\partial X_1}\frac{\partial q_k}{\partial X_j} - (W+T)\frac{\partial q_k}{\partial X_k}\right]dA_0 + \int_{A_0}\left[P_{ji}\frac{\partial^2 U_i}{\partial X_j \partial X_k} - \frac{\partial W}{\partial X_k}\right]q_k\,dA_0 + \int_{A_0}\left[\rho\frac{\partial^2 U_i}{\partial t^2}\frac{\partial U_i}{\partial X_1}q_k - \rho\frac{\partial U_i}{\partial t}\frac{\partial^2 U_i}{\partial X_1 \partial t}q_k\right]dA_0 \quad (30)$$

where W and T are stress-work density and kinetic energy density respectively.

Figure 17 shows the problem definition in which the X coordinate coincides with the fiber orientation in the composites. The full mesh and the five contours used to evaluate the dynamic integral J' are shown in Figure 18. Finite element analyses were performed at five different impact velocities of 5, 10, 20, 30, and 40 m/s.

Figure 19 shows the evolution of crack length and crack speed gained from the simulations of a frictionless crack wake. After initiation, the crack tip accelerates and then attains steady state speed before stopping or before interacting with waves reflected at boundaries. It is found that this model predicts intersonic crack propagation, in the investigated unidirectional fiber composite, when the impact velocity is in excess of 10 m/s. For the impact velocities of 20, 30, and 40 m/s, the crack speed reaches a steady state in the intersonic regime and the maximum speeds are approximately all the

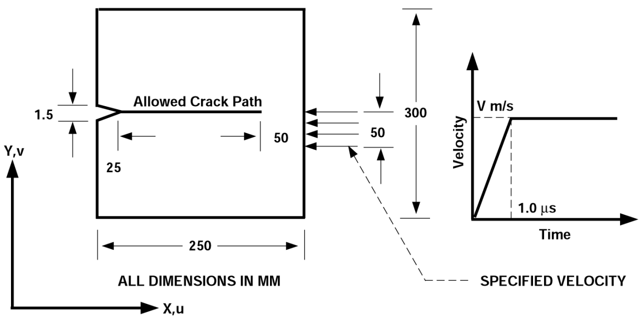

Figure 17: Problem definition of dynamic crack propagation in unidirectional fiber reinforced composite and the specified impact velocity.

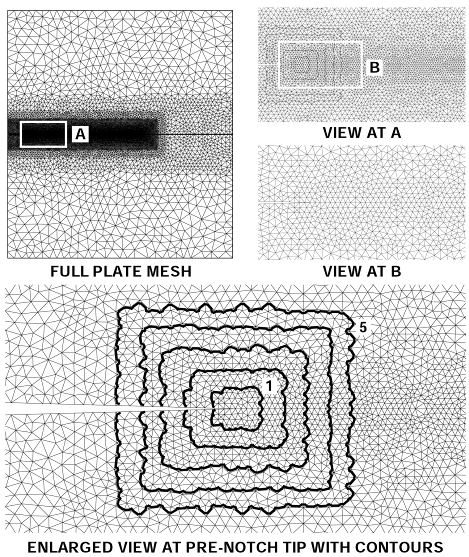

Figure 18: Finite element mesh and contours for J' calculation.

same at 3.9 times the shear wave speed and 83% of the longitudinal wave speed of the material. In the case of subsonic crack propagation, the crack initiates under mixed mode loading due to inherent anisotropy and propagates at a steady state in predominantly mode II. On the other hand, mode II loading is dominant at the onset of intersonic crack propagation. The steady state intersonic crack propagation occurs prevalently under mode II loading even though the crack tip loading is in mixed mode. The most important result is that shock waves, which result from the crack propagating at a speed higher than the material shear and surface waves, are captured as shown in Figure 20. The line of stress discontinuity cannot be observed in the subsonic crack propagation. Formation of shock waves is dependent on the interface properties and boundary conditions.

The analyses predict contact behind intersonically propagating crack tips. Figure 21 shows longitudinal stress contours for the cases of 5 m/s and 40 m/s impact velocities at the onset of crack initiation and at the instant of maximum crack speed. For the 5 m/s impact velocity, the crack front remains open throughout the event because of tensile normal tractions. By contrast, compressive normal tractions are observed behind the intersonically propagating crack tip at 40 m/s impact velocity and contact takes place in the crack faces behind the crack tip. Analyses, which account for friction effects on the crack surfaces, where the contact occurs, were performed with friction coefficients of 0.0, 0.5, 1.0, 5.0, and 10.0 for the impact velocities of 30 and 40 m/s. Although the effect of friction is not discernible on the maximum crack speed at a steady state, its effect is significant concerning the time required to reach steady state propagation. As

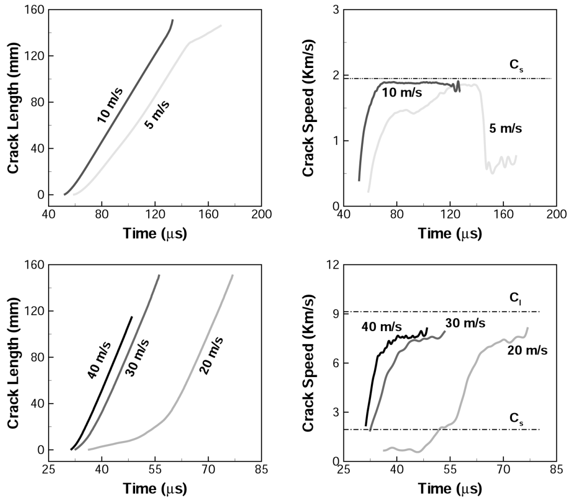

Figure 19: Evolution of crack length and crack speed different impact velocities.

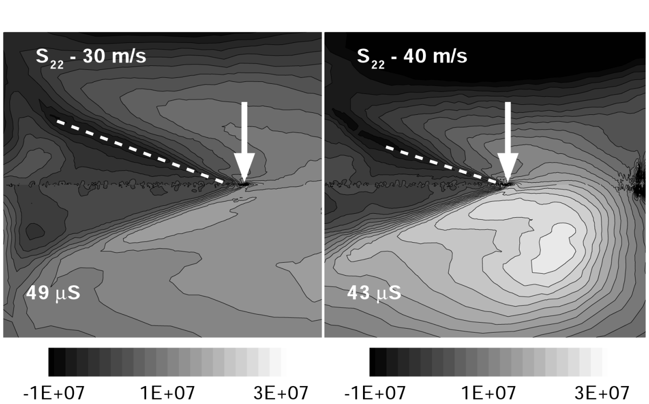

Figure 20: Shock wave, line of stress discontinuity, emanating from the crack tip propagating at intersonic speed at the impact velocities of 30 m/s and 40 m/s.

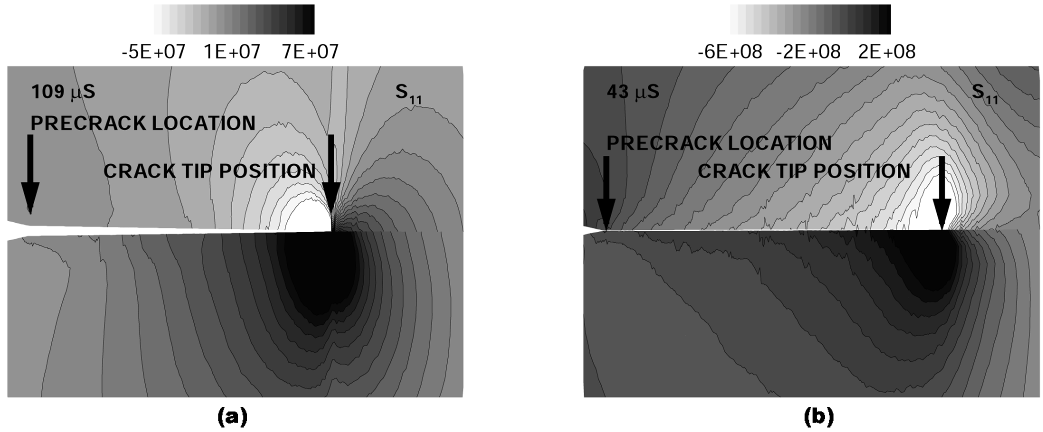

Figure 21: (a) Open crack front for the case of 5 m/s impact velocity (b) closed crack front for the case of 40 m/s impact velocity.

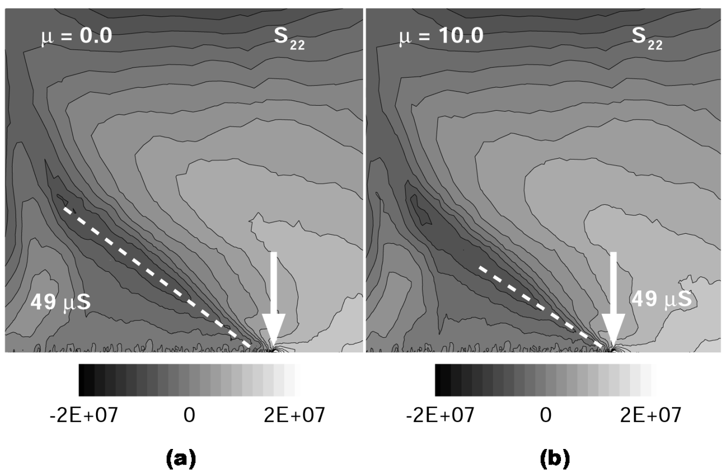

Figure 22: Shock waves at impact velocity of 30 m/s (a) for frictionless crack surfaces (b) with consideration of friction coefficient of 10.0.

shown in Figure 22, the inclination of the discontinuity line increases with the increase of friction, because the friction spreads the region of compressive stress over a larger area in front of the crack tip. Also the integral J' is found constant for near field contours during the steady state crack propagation phase. The presented simulations show that the proposed model adequately predicts the phenomena of dynamic crack propagation in fiber reinforced composite materials. Most of the features observed experimentally are captured in the simulations. Moreover, computed values of J' indicate that this parameter can be used to predict dynamic crack behavior in composites when the decohesion energy is unknown.

4 CONCLUDING REMARKS

Recently, there have been significant advances in computational modeling of ceramic materials and fiber reinforced composites. To understand failure mechanisms in these advanced materials, modeling with augmented finite elements was pursued. Models, which can describe various mechanisms resulting in dynamic failure, were here presented in some detail. Finite deformation inelasticity and visco-plasticity incorporating thermal softening were formulated and implemented in the in-house code FEAP-2000. For ceramic materials, an anisotropic elastic grain level model with automatic mesh generation and random crystal axes orientations was discussed. The generation of polycrystalline ceramic microstructures, which is suitable for grain level analysis, was developed with the aid of Voronoi tessellation and interface elements. An anisotropic plasticity model was proposed for fiber reinforced composite materials. Excessive distortion in the FEM mesh was resolved using mesh adaptivity and consistent mesh transfer operators. Interface cohesive laws were used to simulate crack initiation, crack evolution, and delamination. The interface elements which behave according to the cohesive law were embedded along the possible crack path such as grain boundaries, interface between laminae of composites, and interface between two different materials.

Soft-recovery normal impact experiments were analyzed to obtain insights into damage mechanisms in ceramic materials. The numerically computed particle velocity at the rear surface of the momentum trap plate were in good agreement with the velocities measured experimentally. In particular, the simulation can reproduce the pull-back signal as well as the attenuation of the second compressive pulse as observed in the experiments. It has been found that grain morphology and strength distribution play important roles in capturing the proper microcrack initiation and fragmentation kinetics in view of crack speed and path in real microstructures. The calculation with real microstructures provided a better understanding of different inelastic mechanisms controlling macroscopic behavior. Also we confirmed that there are no rate effects in grain boundary failure of ceramic materials.

In order to study the dynamic shearing resistance of ceramic materials, numerical studies were conducted on pressure shear impact soft recovery experiments. The comparison of transverse velocity obtained from experiments and simulations shows that the frictional sliding between flyer, target and specimen plates controls the traction history at the interface. Roughness characteristics and material properties are key in capturing the physics. The computational model is capable of reproducing the transverse peak velocity, of about 20 m/s, and the progressive reduction in transverse velocity observed in the experiments. It has been also found that inelasticity and thermal softening at the surfaces of the steel plates is a major contributing deformation mechanism. In the full-scale simulations, velocity profiles were found to be in excellent agreement with the experimental results when known steel parameters were used. These micromechanical simulations are useful for quantifying and determining dominant failure mechanisms, as well as deriving damage evolution equations used in continuum and discrete models.

The constitutive response of fiber composite materials and their behavior under impact loading were also studied. Numerical results of off-axis tension tests and compression tests with the postulated anisotropic visco-plastic model was found to agree well with experimental measurements. To analyze damage evolution in GRP composites subjected to impact loading, simulations of ballistic penetration of GRP composites were performed. Modes of energy dissipation were investigated to understand the energy absorption mechanisms in GRP plates. It was found that the inelastic deformation of the composite absorbs significant portions of the total internal energy stored in the GRP plate. The delamination energy increases with an increase in the number of laminae but overall is quite small.

By employing the developed models, dynamic crack propagation in unidirectional composite materials was also analyzed. Most of the features observed experimentally and analytically were captured in these simulations. The computational analyses show that steady state *intersonic* crack propagation can be reached at a speed of 3.9 times the shear wave speed of the material when a threshold energy level is delivered to the crack. It has been also found that the presented computational methodology can be applied to a variety of problems which require consideration of contact and friction behind the intersonically propagating crack tip.

In summary, we conclude that the effects of various fracture mechanisms can be described with the proposed models. The computational models are useful for capturing dynamic fragmentation of ceramic microstructures, material pulverization, and delamination and fracture in fiber composite materials. The cohesive laws incorporated in interfaces and grain boundaries simulate crack nucleation, initiation, propagation and coalescence, as well as crack interaction, contact/friction and crack branching. It was also shown that grain level micromechanical models taking into account stochasticity of microstructures and sliding friction at interfaces is a powerful computational tool. In the analyses of crack propagation in composite materials, friction behind the crack tip was predicted and a shock wave structure emanating from the crack tip observed. The simulation results were found to be in excellent agreement with experimental observations by Coker and Rosakis (2001). The analyses proved that this computational methodology provides tools and means to identify dynamic failure behavior of advanced materials in numerous applications.

Current research in this field is concerned with bridging atomistic scales to macro scales for multiscale analysis. Grain level models with cohesive interfaces are used for the analysis of ceramic materials, spanning from micro to macro scales. Interface elements can also establish the relationship between the homogenization of composite material properties and the micromechanical models of matrices and fibers in composites. Another application of the discussed models, we are currently pursuing, is in the study of thin films and MEMS structures where the material microstructure needs to be accounted for and where surface features are key to the device mechanical behavior.

5 ACKNOWLEDGMENTS

This research was supported by the Purdue Research Foundation through Grant No. 690-1282-2001, the Army Research Office through ARO-MURI Award No. DAAH04-96-1-0331, the Army Office of Scientific Research through Grant Nos. DAAH 04-95-1-0168, DAAH04-96-1-0142, the National Science Foundation through Grant Nos. MSS-9309006, MSS-9311289, Career Award Nos. CMS-9523113, CMS-9624364, the Office of Naval Research YIP through Award No. N00014-97-1-0550, and the Air Force Office of Scientific Research through Award No. F49620-98-1-0039. The support of ARO and DoD HPCMP in providing supercomputer time on the 128 processors Origin 2000 at the Naval Research Laboratory - DC (NRL-DC) is gratefully acknowledged.

The authors would like to thank Dr. Dwivedi and Dr. Zavattieri for their significant contribution to the micro scale modeling of failure mechanisms in ceramics and fiber composites.

6 REFERENCES

Coker, D. and Rosakis, A.J., 2001, Experimental Observations of Intersonic Crack Growth in Asymmetrically Loaded Unidirectional Composite Plates, *Philosophical Magazine A*, **81**, 571-595.

Dwivedi, S.K. and Espinosa, H.D., 2001, Modeling Intersonic Crack Propagation in Fiber Reinforced Composites with Contact/Cohesive Laws, *Damage Initiation and Prediction in Composites, Sandwich Structures and Thermal Barrier Coatings*, edited by A.M. Waas and J.D. Whitcomb, the 2001 ASME International Mechanical Engineering Congress and Exposition, November 11-16, New York, NY, AD-Vol. **66**, 121-153.

Dwivedi, S.K. and Espinosa, H.D., 2002, Modeling dynamic crack propagation in fiber reinforced composites including frictional effects, in print in *Mechanics of*

Materials.

Espinosa, H.D., 1995, On the dynamic shear resistance of ceramic composites and its dependence on applied multiaxial deformation, *International Journal of Solids and Structures*, **32**(21), 3105-3128.

Espinosa, H.D., Zavattieri, P.D., and Dwivedi, S.K., 1998a, A finite deformation continuum/discrete model for the description of fragmentation and damage in brittle materials, *Journal of the Mechanics and Physics of Solids*, **46**(10), 1909-1942.

Espinosa, H.D, Zavattieri, P.D, and Emore, G.L., 1998b, Adaptive FEM computation of geometric and material nonlinearities with application to brittle failure, *Mechanics of Materials*, **29**, 275-305.

Espinosa, H.D., Dwivedi, S.K., and Lu, H.-C., 2000, Modeling impact induced delamination of woven fiber reinforced composites with contact / cohesive laws, *Computer Methods in Applied Mechanics and Engineering*, **183**(3-4), 259-290.

Espinosa, H.D, Lu, H.-C., Zavattieri, P.D., and Dwivedi, S.K., 2001, A 3-D finite deformation anisotropic visco-plasticity model for fiber composites, *Journal of Composite Materials*, **35**(5), 369-410.

Espinosa, H.D., and Zavattieri, P.D., 2002a, A grain level model for the study of failure initiation and evolution of polycrystalline brittle materials. Part I: theory and numerical interpretation, in print in *Mechanics of Materials*.

Espinosa, H.D., and Zavattieri, P.D., 2002b, A grain level model for the study of failure initiation and evolution of polycrystalline brittle materials. Part II: numerical examples, in print in *Mechanics of Materials*.

Zavattieri, P.D., and Espinosa, H.D., 2001, Grain level analysis of crack initiation and propagation in brittle materials, *Acta Materialia*, **49**(20), 4291-4311.

Zavattieri, P.D., and Espinosa, H.D., 2002, Grain level analysis of the frictional behavior of ceramic microstructures subjected to dynamic compression-shear loading, in print in *Journal of the Mechanics and Physics of Solids*.